Blob dynamics in the TORPEX experiment: a multi-code validation

F. Riva,[1, a)] C. Colin,[2] J. Denis,[2, 3] L. Easy,[4, 5] I. Furno,[1] J. Madsen,[6] F. Militello,[5] V. Naulin,[6] A. H. Nielsen,[6] J. M. B. Olsen,[6] J. T. Omotani,[5] J. J. Rasmussen,[6] P. Ricci,[1] E. Serre,[2] P. Tamain,[3] and C. Theiler[1]

[1)] *École Polytechnique Fédérale de Lausanne (EPFL), Swiss Plasma Center (SPC), CH-1015 Lausanne, Switzerland*

[2)] *Aix Marseille Université, CNRS, Centrale Marseille, M2P2 UMR 7340, 13451, Marseille, France*

[3)] *CEA, IRFM, F-13108 Saint-Paul-lez-Durance, France*

[4)] *Department of Physics, University of York, Heslington, York YO10 5DD, United Kingdom*

[5)] *CCFE, Culham Science Centre, Abingdon OX14 3DB, United Kingdom*

[6)] *Deparment of Physics, Technical Univervsity of Denmark, Kgs. Lyngby, Denmark*

Three-dimensional and two-dimensional seeded blob simulations are performed with five different fluid models, all based on the drift-reduced Braginskii equations, and the numerical results are compared among themselves and validated against experimental measurements provided by the TORPEX device [A. Fasoli *et al.*, Phys. Plasmas **13**, 055902 (2006)]. The five models are implemented in four simulation codes, typically used to simulate the plasma dynamics in the tokamak SOL, namely BOUT++ [B. Dudson *et al.*, Comput. Phys. Commun. **180**, 1467 (2009)], GBS [P. Ricci *et al.*, Plasma Phys. Control. Fusion **54**, 124047 (2012)], HESEL [A. H. Nielsen *et al.*, Phys. Lett. A **379**, 3097 (2015)], and TOKAM3X [P. Tamain *et al.*, Contrib. Plasma Phys. **54**, 555 (2014)]. Three blobs with different velocities and different stability properties are simulated. The differences observed among the simulation results and the different levels of agreement with experimental measurements are investigated, increasing our confidence in our simulation tools and shedding light on the blob dynamics. The comparisons demonstrate that the radial blob dynamics observed in the three-dimensional simulations is in good agreement with experimental measurements and that, in the present experimental scenario, the two-dimensional model derived under the assumption of $k_{\parallel} = 0$ is able to recover the blob dynamics observed in the three-dimensional simulations. Moreover, it is found that an accurate measurement of the blob temperature is important to perform reliable seeded blob simulations.

[a)] Electronic mail: fabio.riva@epfl.ch

I. INTRODUCTION

The understanding of the plasma dynamics in the Scrape-Off Layer (SOL) of tokamaks is of crucial importance as we approach the ITER[1] era. Particles and heat cross the separatrix from the core via turbulent transport to enter this region, whereupon they flow along the magnetic field lines and are ultimately exhausted to the vessel. The processes taking place in the SOL govern the performance of the entire fusion device, as they determine the impurity dynamics, the recycling level, the peak heat loads at the vessel, and have an important role in setting the overall plasma confinement.

While in the SOL region a wide range of different turbulent phenomena are present, in this paper we focus on the study of blobs. Blobs, also known as filaments, are structures with an excess of density and temperature relative to the surrounding plasma, elongated in the direction parallel to the magnetic field. Blobs detach from the main plasma and move outwards due to a self-generated $\mathbf{E} \times \mathbf{B}$ field. Experimental evidences point out that the transport associated with these structures could reach half of the total transport observed in a tokamak SOL[2], leading to significant particle and heat fluxes to the walls. In the recent past, a large effort has been carried out to improve the knowledge of the blob dynamics, both experimentally and theoretically, achieving significant progress[2,3].

The goal of the present paper is to improve our understanding of the blob dynamics, and therefore the reliability of their simulations, performing a common validation project involving several plasma turbulence codes used to model the SOL region. In fact, despite their large use in analyzing the blob dynamics (see, e.g., Refs. [4–12]), a detailed validation project of seeded blob simulations has not been carried out yet. Herein, two-dimensional and three-dimensional simulations of seeded blobs, based on five different models implemented in four turbulence codes (BOUT++[13], GBS[14], HESEL[15,16], and TOKAM3X[17]), are validated against experimental blob measurements. We assess the consistency of the numerical results with experimental measurements and, at the same time, we investigate the differences between the simulation results of the five models through a benchmark study. Thanks to the differences among the models, we identify and assess the key physics elements that determine the blob motion.

The experimental measurements are taken from the TORPEX[18,19] experiment, an ideal device for the validation of plasma turbulence codes. In fact, the TORPEX configuration

mimics the main features of the tokamak SOL, while remaining relatively simple, and it is equipped with a complete set of diagnostics. Conditionally-averaged measurements taken on TORPEX provide the two-dimensional profiles of plasma density, electron temperature, and electrostatic potential for the blob, which are needed to accurately initialize seeded blob simulations. At the same time, it also provides the measurement of the blob velocity used to validate the numerical results. A parameter scan is performed by detecting blobs with different density peak values. This allows for a comparison between experimental measurements and simulations of blobs propagating at different velocities and having different internal stability properties.

Because of the relatively high collisionality of the TORPEX plasma, all models we consider are based on the drift-reduced Braginskii equations. However, they differ in the assumptions used to simplify the equations, such as the hypothesis of cold ions, isothermal electrons, or negligible electron inertia. Some of the models make use of the infinite aspect ratio approximation. We also consider two-dimensional models, based on different closures of the parallel currents on the vessel wall. The influence of all these assumptions on the blob dynamics is analyzed through a benchmark study, where the same scenario is considered for all the models, and the differences observed in the simulation results are investigated.

This paper is structured as follows. After this Introduction, in Sec. II we illustrate the TORPEX device and the experimental setup used in the present work. Section III introduces the five models used to simulate the blob dynamics and discusses their main differences. Then, in Sec. IV we illustrate our simulations, focusing on their initialization. Sec. V present a sensitivity study performed to investigate the influence of the input parameter uncertainties on the numerical results. The comparison of the experimental measurements and the simulations are the subject of Sec. VI. The Conclusions follow in Sec.VII.

II. EXPERIMENTAL SCENARIO

The experimental data presented in this work are obtained on the TORPEX experiment, a toroidal device with major radius $R = 1\,\mathrm{m}$ and minor radius $a = 0.2\,\mathrm{m}$ that features the simple magnetized toroidal (SMT) configuration. A toroidal magnetic field ($B_\phi = 76\,\mathrm{mT}$ on axis) superposed on a vertical magnetic field ($B_v = 1.6\,\mathrm{mT}$) results in helical field lines that wind around the device. The field lines intercept the top and bottom walls of the device in

the inner half part of the cross section (high field side), while in the outer half of the cross section (low field size) a poloidal steel limiter provides a region that has a nearly constant connection length $L \simeq 2\pi R$, and near-perpendicular incidence of the magnetic field lines on the target[20]. This configuration is schematically shown in Fig. 1(a). The coordinate system (y, x, z) used in this paper is also represented in Fig. 1(a): x is the radial direction, z is the direction parallel to B (and coincides approximatively with the toroidal direction), and y is perpendicular to x and z (and coincides approximatively with the vertical direction).

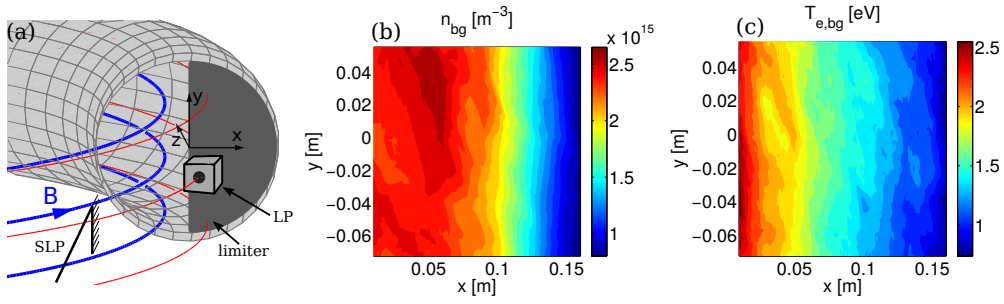

FIG. 1. (a) Schematic representation of the TORPEX experiment. The limiter located in the low-field side region is shown together with the probes used to perform blob conditional sampling. Note that SLP is not represented at 180^o from the limiter as it is in the experiment for drawing convenience. (b-c) Background profiles of n and T_e in the low-field side region, where blobs propagate. The profiles are measured in a poloidal plane 3 cm away from the limiter.

A hydrogen plasma is produced and sustained by microwaves in the electron cyclotron range of frequencies. On the high-field side of the device, turbulence driven by ideal interchange modes[21,22] results in blobs, which dominate transport on the low field side. Typical plasma parameters are $n \simeq 10^{16}\,\mathrm{m}^{-3}$ and $T_e \simeq 5\,\mathrm{eV}$ in the source region, and are slightly smaller in the blob region. The ions are typically much colder than the electrons. An example of the time averaged profiles measured in the blob region is presented in Figs. 1(b-c).

The experimental results used in this paper are obtained using two diagnostics: (i) a vertically oriented linear array of Langmuir probes (LPs) with 1.8 cm distance between tips, located at $x = 7\,\mathrm{cm}$ and toroidally separated approximatively by $180°$ from the limiter, referred to as SLP, and (ii) a single-sided LP, positioned approximatively 3 cm away from the limiter and with the collecting plate oriented perpendicularly to the magnetic field lines.

Time-resolved two-dimensional measurements associated with blobs are obtained using conditional sampling over many blob events, allowing the reconstruction of the I-V Langmuir characteristic. This technique is explained in details in Ref. [21], and can be summarized as follows. The probes of the SLP array, biased at $-40\,\mathrm{V}$ and operated in ion saturation current mode, are located at fixed positions in the blob region and are used as reference probes, while the single-sided probe, placed close to the limiter, is operated in swept mode. Positive bursts in the SLP reference signals are interpreted as blobs moving in front of the reference probe. When a blob is detected, the voltage V applied to the swept probe and the corresponding measured current value I are retained. The whole set of voltage and current values is interpreted as the I-V characteristic associated with blobs, which is evaluated as a function of time with respect to the detection. To reconstruct the two-dimensional profiles, the single-sided LP is moved radially in between discharges. This experimental setup has been used to investigate the parallel current structure associated with blobs, as presented in Ref. [10].

The TORPEX experiment is an ideal device for the validation of plasma turbulence codes for two reasons. First, a wide range of observables can be provided with high spatial resolution, such as the plasma density, the electron temperature, the floating potential, and the parallel current. This is crucial to perform accurate seeded blob simulations, which require the profiles of all evolved fields at a certain time to set the proper initial conditions. Second, the SMT configuration mimics the main features of the tokamak SOL, such as open field lines, curvature and gradients of the magnetic field, and plasma pressure gradients, but in a simpler configuration. This facilitates considerably the analysis and the interpretation of the experimental and simulation results.

III. THE MODELS AND THE SIMULATION CODES

Because of the relatively high collisionality of TORPEX plasmas, we use a fluid approach based on the Braginskii equations[23] to model the blob dynamics. Moreover, since the time scale of the blob dynamics is such that $d/dt \ll \omega_{ci}$ (where $\omega_{ci} = eB/m_i$ is the ion gyrofrequency), we can consider these equations in the drift limit[24]. Finally, we note that, since in the present scenario magnetic perturbations are negligible, only electrostatic models are

considered.

Although the drift-reduced Braginskii model is now well established, for practical purposes several approximations are introduced to simplify the equations. Those approximations vary from code to code and, in general, their effect on the blob motion is not well known. In order to evaluate their impact on the blob dynamics, while identifying the physical processes that play the most important role in setting the blob motion, we perform several seeded blob simulations by using five different non-linear models, implemented in four different simulation codes, each of which is used to simulate the plasma dynamics in the tokamak SOL. The five models are: two isothermal models, one three-dimensional and the other one two-dimensional, written in the STORM module[11] within the BOUT++ framework[13] and named in the following BOUT++3D and BOUT++2D, a three-dimensional cold ion model implemented in the GBS code[14], a two-dimensional model implemented in the HESEL code[15,16], and a three-dimensional isothermal model implemented in the TOKAM3X code[17]. In the remainder of this section, each of the simulation models and codes is described and a discussion of the differences between the models is provided.

All the equations presented in the following of this section are normalized according to Bohm normalization (tilde denotes a dimensional quantity): $\tilde{n} = nn_0$, $\tilde{v}_{\parallel i} = v_{\parallel i}c_{s0}$, $\tilde{v}_{\parallel e} = v_{\parallel e}c_{s0}$, $\tilde{T}_e = T_{e0}T_e$, and $\tilde{\phi} = \phi T_{e0}/e$, where n represents the plasma density, $v_{\parallel i}$ and $v_{\parallel e}$ the ion and electron parallel velocity, T_e the electron temperature, and ϕ the electrostatic potential. Moreover, n_0 and T_{e0} are the reference density and electron temperature, while the normalization quantities c_{s0} and ρ_{s0} are defined as $c_{s0} = \sqrt{T_{e0}/m_i}$ and $\rho_{s0} = c_{s0}/\omega_{ci}$, where $\omega_{ci} = eB_0/m_i$. The magnetic field B is normalized to its value on axis, B_0, while time and length scales are normalized to ω_{ci}^{-1} and ρ_{s0}, respectively.

Additionally, the following notations are used: $j_\parallel = n\left(v_{\parallel i} - v_{\parallel e}\right)$ is the parallel current, m_i/m_e is the ion to electron mass ratio, $R = \tilde{R}/\rho_{s0}$ is the TORPEX major radius in normalized units, $\omega = \nabla_\perp^2\phi$ is the vorticity, $p_e = nT_e$ is the electron pressure, $B = 1/(1+x)$ is the magnetic field amplitude in normalized units, $\mathbf{b} = \mathbf{B}/B$ is the unitary vector parallel to $\mathbf{B}$, $\nabla_\parallel = \mathbf{b}\cdot\nabla$ is the parallel gradient, and $[A, B] = \mathbf{b}\cdot(\nabla A \times \nabla B)$.

A. BOUT++3D

Assuming cold ions and isothermal electrons, and considering the infinite aspect ratio limit (in particular $\nabla \cdot \mathbf{b} = 0$), the BOUT++3D drift-reduced Braginskii equations in normalized units can be written as:

$$\frac{d^0 n}{dt} + nC(\phi) - C(n) = -\nabla_\parallel \left(n v_{\parallel e}\right) + \mathcal{D}_n(n) + S_n \tag{1}$$

$$\frac{d^0 \omega}{dt} - \frac{C(n)}{n} = -v_{\parallel i}\nabla_\parallel \omega + \frac{\nabla_\parallel j_\parallel}{n} + \mathcal{D}_\omega(\omega) \tag{2}$$

$$\frac{d^0 v_{\parallel i}}{dt} = -v_{\parallel i}\nabla_\parallel v_{\parallel i} - \nabla_\parallel \phi - \eta_\parallel j_\parallel - \frac{S_n v_{\parallel i}}{n} \tag{3}$$

$$\frac{d^0 v_{\parallel e}}{dt} = -v_{\parallel e}\nabla_\parallel v_{\parallel e} + \frac{m_i}{m_e}\left(\nabla_\parallel \phi - \frac{\nabla_\parallel n}{n} + \eta_\parallel j_\parallel\right) - \frac{S_n v_{\parallel e}}{n} \tag{4}$$

Here $d^0 f/dt = \partial_t f + [\phi, f]$ is the convective derivative that takes into account the $\mathbf{E} \times \mathbf{B}$ drift, $C(f) = -g\partial_y f$ is the curvature operator, where $g = 2/R$ represents the strength of the ∇B and curvature drifts, S_n is a particle source [see Sec. IV, Eq. (22) for its definition], $\eta_\parallel = m_e \nu_{ei}/(1.96 m_i \omega_{ci})$ is the normalized parallel resistivity, $\nu_{ei} = n_0 e^4 \ln\Lambda / \left[3 m_e^{1/2} \epsilon_0^2 \left(2\pi T_{e0}\right)^{3/2}\right]$ is the electron-ion collision frequency, $\mathcal{D}_n(n) = D_n \nabla_\perp^2 n$ and $\mathcal{D}_\omega(\omega) = \mu_i \nabla_\perp^2 \omega$ are perpendicular diffusion operators, where $D_n = 2 m_e \nu_{ei}/(m_i \omega_{ci})$ and $\mu_i = 3\nu_{ei}/(4\omega_{ci})\sqrt{m_e/m_i}$ are the normalized particle perpendicular diffusivity and the normalized ion perpendicular viscosity respectively. We note that in all the codes the Boussinesq approximation is used to simplify the evaluation of the divergence of the polarization current (the validity of this assumption in modelling the SOL plasma dynamics is discussed in Refs. [25–27]).

The system of equations (1-4), supplemented by standard sheath boundary conditions[28] [i.e., $v_{\parallel i} = \pm 1$ and $v_{\parallel e} = \pm \exp(-\phi)$ at the target], constitutes the BOUT++3D model, which is implemented within the BOUT++ framework. A first order upwinding scheme is employed to evaluate the parallel advection derivatives, while the Arakawa scheme[29] is used for the perpendicular $\mathbf{E} \times \mathbf{B}$ advective derivatives. Other derivatives are computed using second order central difference schemes. Time integration is carried out with a variable time-step, variable order, fully implicit Newton-Krylov backwards difference formula solver from the PVODE library[30]. We note that only half of the physical domain is evolved, assuming a symmetric evolution of the blobs with respect to the plane perpendicular to the magnetic field that is midway between the two limiter surfaces. A more detailed discussion of the

model is presented in Ref. [11].

B. BOUT++2D

Assuming $k_\parallel = 0$ and linearizing the sheath boundary conditions, such that $v_{\parallel e} = \pm \exp(-\phi) \simeq \pm(1-\phi)$, the system of equations (1-4) can be integrated in the parallel direction, in order to evolve line-averaged quantities. Consequently, the three-dimensional system of equations reduces to the following two-dimensional fluid equations:

$$\frac{d^0 n}{dt} + nC(\phi) - C(n) = -2\frac{n(1-\phi)}{L_\parallel} + \mathcal{D}_n(n) + S_n \tag{5}$$

$$\frac{d^0 \omega}{dt} - \frac{C(n)}{n} = 2\frac{\phi}{L_\parallel} + \mathcal{D}_\omega(\omega) \tag{6}$$

Here $L_\parallel = 2\pi R$ is the connection length in normalized units and $S_n = 2n_{bg}/L_\parallel$ is a particle source [see Sec. IV, Eq. (20) for the definition of n_{bg}]. The quantities n, ω, and ϕ are the line-averaged plasma density, vorticity, and electrostatic potential respectively, and, taking n as an example, are defined as $n(x,y) = \int_0^{L_\parallel} n(x,y,z)dz/L_\parallel$.

Eqs. (5-6) constitute the BOUT++2D model, which is implemented within the BOUT++ framework. For its solution, the same numerical scheme employed in BOUT++3D is used. For a more detailed discussion of this model see Ref. [11].

C. GBS

Assuming cold ions and considering the infinite aspect ratio limit, the drift-reduced Braginskii equations implemented in the GBS code are:

$$\frac{d^0 n}{dt} + nC(\phi) - C(p_e) = -\nabla_\parallel \left(n v_{\parallel e}\right) + \mathcal{D}_n(n) + S_n \tag{7}$$

$$\frac{d^0 \omega}{dt} - \frac{C(p_e)}{n} = -v_{\parallel i}\nabla_\parallel \omega + \frac{\nabla_\parallel j_\parallel}{n} + \mathcal{D}_\omega(\omega) + \frac{C(G_i)}{3n} \tag{8}$$

$$\frac{d^0 v_{\parallel i}}{dt} = -v_{\parallel i}\nabla_\parallel v_{\parallel i} - \frac{\nabla_\parallel p_e}{n} - \nu_{in} v_{\parallel i} + \mathcal{D}_{v_{\parallel i}}(v_{\parallel i}) - \frac{2\nabla_\parallel G_i}{3n} \tag{9}$$

$$\begin{aligned}\frac{d^0 v_{\parallel e}}{dt} = &-v_{\parallel e}\nabla_\parallel v_{\parallel e} - \nu_{en} v_{\parallel e} + \mathcal{D}_{v_{\parallel e}}(v_{\parallel e}) \\ &+ \frac{m_i}{m_e}\left(\nabla_\parallel \phi - \frac{\nabla_\parallel p_e}{n} - 0.71 n \nabla_\parallel T_e + \eta_\parallel j_\parallel - \frac{2\nabla_\parallel G_e}{3n}\right)\end{aligned} \tag{10}$$

$$\begin{aligned}\frac{d^0 T_e}{dt} + \frac{2}{3}T_e\left[C(\phi) - \frac{5}{2}C(T_e) - \frac{C(p_e)}{n}\right] = &-v_{\parallel e}\nabla_\parallel T_e + \frac{2}{3}T_e\left(0.71\frac{\nabla_\parallel j_\parallel}{n} - \nabla_\parallel v_{\parallel e}\right) \\ &+ \mathcal{D}_{T_e}(T_e) + S_{T_e}\end{aligned} \tag{11}$$

The normalized ion-neutral and electron-neutral collision frequencies, ν_{in} and ν_{en}, evaluated as described in Ref. [31], are introduced here to mimic collisions with the neutral particles present in a weakly ionized plasma, such as that found in TORPEX. The terms S_n and S_{T_e} are the particle and electron temperature sources, respectively. Small perpendicular diffusion terms, written in the form $\mathcal{D}_a(a) = D_a \nabla_\perp^2 a$, where D_a are constant coefficients, are introduced mainly for numerical reasons. The two terms representing gyroviscous effects are given by $G_i = -\eta_{0i}\left[2\nabla_\parallel v_{\parallel i} + C\left(\phi\right)\right]$ and $G_e = -\eta_{0e}\left[2\nabla_\parallel v_{\parallel e} - C\left(p_e\right)/n + C\left(\phi\right)\right]$.

Equations (7-11), supplemented by Bohm's boundary conditions [i.e., $v_{\parallel i} = \pm c_s$ and $v_{\parallel e} = \pm c_s \exp\left(\Lambda - \phi/T_e\right)$ at the sheath entrance, where $c_s = \sqrt{T_e}$ and $\Lambda = 3$ for hydrogen plasmas], constitute the GBS model. Spatial derivatives are discretized using a second-order finite difference scheme, except for the $\mathbf{E} \times \mathbf{B}$ advective terms, which are discretized with a second-order Arakawa scheme. Time is advanced using a standard fourth-order Runge-Kutta scheme. For a more detailed discussion of the GBS code, see Ref. [14].

In the present work, all fields have been separated into background and seeded blob

components, and only the latter component is evolved. This allows us to use arbitrary background profiles, with no need to find and implement the appropriate plasma source. To clarify this procedure, we rewrite Eq. (7) in the form that is actually solved by GBS:

$$\begin{aligned}\frac{\partial n_{bl}}{\partial t} =& -[\phi_{bg}, n_{bl}] - [\phi_{bl}, n_{bg}] - [\phi_{bl}, n_{bl}] + \mathcal{D}_n(n_{bl}) \\ &+ (T_{e,bg} + T_{e,bl})C(n_{bl}) + (n_{bg} + n_{bl})\left[C(T_{e,bl}) - C(\phi_{bl})\right] \\ &- (n_{bg} + n_{bl})\nabla_\parallel v_{\parallel e,bl} - n_{bl}\nabla_\parallel v_{\parallel e,bg} - (v_{\parallel e,bg} + v_{\parallel e,bl})\nabla_\parallel n_{bl} - v_{\parallel e,bl}\nabla_\parallel n_{bg}\end{aligned} \tag{12}$$

where the indexes *bg* and *bl* refer to the background and blob components, respectively. In Eq. (12) it has been assumed that the background profiles are constant in time and independent of y. Equations (8-11) and Bohm's boundary conditions are treated with the same procedure.

It has been verified with a two-dimensional version of the GBS model that there are no significant differences between seeded blob simulations carried out by separating the background and blob quantities with respect to the ones where they are both evolved simultaneously.

D. HESEL

In the HESEL model, the drift-reduced Braginskii equations are reduced to a set of two-dimensional fluid equations by neglecting the instantaneous parallel currents, while retaining the equilibrium one, and estimating the parallel advection terms under the hypothesis $v_{\parallel i}\nabla_\parallel = v_{\parallel e}\nabla_\parallel \approx c_s/L_\parallel$. The resulting model, which is implemented in the HESEL code, is presented in Refs. [15 and 16]. However, as will be discussed later, the ion temperature dynamics shows a very small impact on the seeded blob simulation results. Therefore, to simplify the discussion of the differences between the models considered in the present paper, we choose to not show here the ion temperature equation and to present only the cold ion model.

Neglecting electron-ion collisions and assuming cold ions, the system of equation presented

in Refs. [15 and 16] reduces to:

$$\frac{d}{dt}n + n\hat{C}(\phi) - \hat{C}(p_e) = -\frac{n}{\tau_n} + \mathcal{D}_n(n+\phi) \tag{13}$$

$$\nabla\cdot\left(\frac{d^0}{dt}\nabla_\perp\phi\right) - \hat{C}(p_e) = D_\omega(\omega) - \nu_{in}\omega + \frac{2c_s}{L_\parallel}\left[1 - \exp\left(\Lambda - \frac{\langle\phi\rangle_y}{\langle T_e\rangle_y}\right)\right] \tag{14}$$

$$\frac{3}{2}\frac{d}{dt}p_e + \frac{5}{2}p_e\hat{C}(\phi) - \frac{5}{2}\hat{C}\left(\frac{p_e^2}{n}\right) = -\frac{p_e}{\tau_{\parallel,p_e}n} + \frac{3}{2}\mathcal{D}_n(p_e-\phi) \tag{15}$$

Here $df/dt = \partial_t f + [\phi, f]/B$ is the convective derivative and $\hat{C}(f) = -\hat{g}\partial_y f$ is the HESEL curvature operator, with $\hat{g} = 1/R$. Equilibrium currents to the limiter are approximated by the sheath dissipation term entering in Eq. (14), where $\langle - \rangle_y$ represents the average along y, with $\Lambda = 2.8$ in this case. The perpendicular diffusion terms $\mathcal{D}_n(a) = D_{en}\nabla_\perp^2 a$ and $\mathcal{D}_\omega(a) = D_\omega\nabla_\perp^2 a$ are introduced to describe electron-neutral and ion-ion collisions, where $D_{en} = \rho_e^2\nu_{en}$ and $D_\omega = \rho_i^2\nu_{ii}$, ρ_e and ρ_i are respectively the electron and ion Larmor radius in normalized units, and ν_{en} and ν_{ii} are respectively the electron-neutral and the ion-ion collision frequencies in normalized units. The loss of the plasma density due to the parallel flow is parameterized by the characteristic time $\tau_n = L_\parallel/(2c_s)$, while the electron pressure parallel dynamics by $\tau_{\parallel,p_e} = 15L_\parallel^2\nu_{en}\left(1 + 4/\nu_{es}\right)/(128v_e^2)$, where $\nu_{es} = L_\parallel\nu_{en}/(2v_e)$ and v_e is the thermal electron velocity in normalized units. The parallel advection of the vorticity is neglected here, because of its small amplitude with respect to the ion-neutral collisions drag term $\nu_{in}\omega$.

The HESEL model is implemented in the code using the Arakawa scheme to discretize the $\mathbf{E}\times\mathbf{B}$ advective terms, a finite difference scheme to discretize the x and y derivatives, and a stiffly-stable third-order scheme[32] for time integration. A more complete discussion of this code is presented in Refs. [15 and 16].

E. TOKAM3X

Assuming cold ions and isothermal electrons, the version of the drift-reduced Braginskii equations evolved by TOKAM3X can be written as follows:

$$\frac{dn}{dt} + nC(\phi) - C(n) = -\nabla \cdot \left[\left(\Gamma - j_\parallel\right)\mathbf{b}\right] + \mathcal{D}_n(n) + S_n \tag{16}$$

$$\frac{d\Omega}{dt} + \Omega C(\phi) - 2C(n) = \nabla \cdot \left[\left(j_\parallel - \Omega\frac{\Gamma}{n}\right)\mathbf{b}\right] + \mathcal{D}_\Omega(\Omega) \tag{17}$$

$$\frac{d\Gamma}{dt} + \Gamma C(\phi) + C(\Gamma) = -\nabla \cdot \left(\Gamma\frac{\Gamma}{n}\mathbf{b}\right) - 2\nabla_\parallel n + \mathcal{D}_\Gamma(\Gamma) \tag{18}$$

$$n\nabla_\parallel\phi - \nabla_\parallel n + \eta_\parallel n j_\parallel = 0 \tag{19}$$

where $\Omega = \nabla \cdot (\nabla_\perp\phi/B^2)$ is the plasma vorticity that takes into account magnetic field variations, $\Gamma = nv_{\parallel i}$ is the ion parallel momentum and S_n is a particle source [see Sec. IV, Eq. (22) for its definition]. Small perpendicular diffusion terms of the form $\mathcal{D}_a(a) = D_a\nabla_\perp^2 a$, where D_a are constant coefficients, are introduced to dissipate turbulent structures of size comparable to the grid spacing.

Equations (16-19), completed by the linearized Bohm's boundary conditions [i.e., $\Gamma = \pm n$ and $j_\parallel = \pm n\left[1 - \exp\left(\Lambda - \phi\right)\right] \simeq \pm n\left(\phi - \Lambda\right)$ at the target], are solved by the TOKAM3X code with a first order operator splitting. Advection terms and source terms are first advanced explicitly, using a shock-capturing algorithm (i.e, the Roe-Marquina scheme based on the WENO interpolation[33]). Parallel current terms are advanced using a fully implicit three-dimensional solver in order to capture the associated fast dynamics without considerably constraining the time step. Finally, perpendicular diffusion terms are advanced implicitly. The latter choice (versus an explicit treatment) is actually not mandatory for the seeded blob simulations considered here, where low diffusion coefficients are used. The spatial discretization is done based on conservative finite differences evaluated on a structured flux-surface aligned mesh. A more detailed discussion of the TOKAM3X code is presented in Ref. [17].

F. Summary of analogies and differences among the physical models

Besides the differences related to the numerical schemes used to evolve the five models, which are neglected here as we consider simulations that are numerically converged, the five

models differ because of several assumptions made to simplify the drift-reduced Braginskii equations. The remainder of this section is dedicated to a discussion of these differences. To examine the differences between the models, we note that Eqs. (16-19) can be recast in the GBS and BOUT++ form by expressing Ω, Γ and $j_\parallel$ in terms of the quantities evolved by these codes. Moreover, we note that it has been verified with the TOKAM3X code that, in the considered blob scenarios, the Boussinesq approximation has a negligible influence on the numerical results.

(i) Two-dimensional closures. In order to reduce the three-dimensional model to a two-dimensional set of equations, in BOUT++2D we impose the sheath dissipation closure, that is $k_\parallel = 0$[11], while in HESEL we impose the vorticity advection closure by approximating $v_{\parallel i}\nabla_\parallel = v_{\parallel e}\nabla_\parallel \approx c_s/L_\parallel$[11]. By imposing the sheath dissipation closure, one assumes that the parallel gradients are negligible, and that the filament extend from target to target. On the other hand, by applying the vorticity advection closure, instantaneous sheath currents are neglected[11]. In Ref. [11] the influence of these approximation on the blob dynamics is discussed, showing that they can have a very strong impact on the simulation results. This analysis will be used in Sec. VI to interpret the numerical results.

(ii) Boundary conditions. The BOUT++3D and GBS models are supplemented by the full Bohm's boundary conditions, the TOKAM3X and BOUT++2D employ the linearized Bohm's boundary conditions, while the HESEL model makes use of the weak sheath formulation, and therefore the equilibrium currents to the limiter are described by the sheath dissipation term entering in Eq. (14). It has been verified with BOUT++3D that the linearization of the boundary conditions has negligible impact on the simulation results presented herein.

(iii) Temperature effects. In the present work the BOUT++2D, BOUT++3D, and TOKAM3X models assume isothermal electrons and cold ions, GBS assumes cold ions, while HESEL evolves the ions dynamics, assuming ions initially at room temperature ($T_i = 0.025\,\mathrm{eV}$ at $t = 0$). A detailed investigation of the T_e effects on the simulation results is presented in Sec. V. The T_i influence on the simulation results has been investigated with HESEL, showing negligible impact on the blob dynamics, and will not be further discussed.

(iv) Magnetic field equilibrium and background profiles. First, regarding the magnetic geometry, we note that BOUT++2D, BOUT++3D, and GBS are written in the infinite aspect ratio limit, while TOKAM3X retains the $\nabla \cdot \mathbf{b}$ terms. Moreover, in TOKAM3X and HESEL the variation of the magnetic field is retained in the $\mathbf{E} \times \mathbf{B}$ advective terms, while it is neglected in BOUT++2D, BOUT++3D, and GBS. Due to the TORPEX large aspect ratio, these approximations have a negligible influence on the results. We also note that in BOUT++2D, BOUT++3D, GBS, and TOKAM3X models, the curvature operator, $C(-)$, is twice as large as the curvature operator $\hat{C}(-)$ appearing in HESEL (i.e., $g = 2\hat{g}$). Therefore, in HESEL, the ballooning instability drive is halved with respect to the one present in the other four models (a reduced ballooning drive leads to slower blob radial motion[20]). Finally, we note that, in the version of GBS used here the background profiles are time-independent and can be arbitrarily imposed because of the separation between background and blob components, in BOUT++2D, BOUT++3D, and TOKAM3X the full quantities are evolved, and the equilibrium profiles are sustained by appropriate source terms, while in HESEL the full quantities are evolved, but, assuming slow variation of the plasma background with respect to the time-scale evolution of blobs, no source terms are introduced to sustain the background profiles (this is justified a posteriori by the simulation results).

(v) Electron inertia. In BOUT++3D the electron inertia is retained in both the parallel ion and electron momentum equations [Eqs. (3-4)], in GBS it is neglected in the ion parallel momentum equation [Eq. (9)], while in TOKAM3X it is neglected in both equations [Eqs. (18-19)]. As a matter of fact, the simulations presented in Sec. VI show that the electron inertia has negligible influence on the blob motion.

(vi) Dissipative terms. In BOUT++2D, and BOUT++ 3D, the perpendicular diffusion coefficients are set using the physical values of the electron-ion and ion-ion collision frequencies, whilst in HESEL, electron-neutral and ion-neutral collisions are also taken into account. These classical diffusion coefficients are computed accordingly to Ref. [34]. In contrast, in GBS and TOKAM3X arbitrary perpendicular dissipative terms are introduced ($D_a \simeq 5 \cdot 10^{-4} - 10^{-3}$), and we have ensured that they have a negligible influence on the

simulation results using GBS to perform a sensitivity scan of the diffusion coefficients over two orders of magnitude, i.e., decreasing and increasing the value of the diffusion coefficients used for the simulation by a factor of ten. Moreover, in GBS the ν_{en} and ν_{in} terms are introduced to mimic the electron-neutral and ion-neutral collisions, while the G_e and G_i terms model the plasma viscosity. A sensitivity scan of these dissipative coefficients over two orders of magnitude show that they have a negligible impact on the simulation results.

In Sec. V and VI we discuss the influence of the approximations listed above on the blob dynamics, comparing the simulations performed with the five models among themselves and against experimental data. In particular, we identify the modeling of the electron temperature and the parallel current closure used to derive the two-dimensional models as the most important differences among the models, and therefore, we focus our attention on those.

IV. SEEDED BLOB SIMULATIONS

Using the five models presented in Sec. III, we perform simulations of seeded blob motion with three different sets of initial conditions. This allows us to compare the simulations among themselves and validate them against experimental observations over a set of different conditions. The three different cases correspond to considering three different amplitude windows for the blob detection in the I_{sat} reference signal provided by the SLP tips. More precisely, we consider trigger events for which the I_{sat} peaks of the reference signal fall in (i) the interval $2.0\sigma - 2.75\sigma$, where σ is the standard deviation of the reference signal ($\sigma/\langle I_{sat}\rangle_t \approx 0.5$, where $\langle I_{sat}\rangle_t$ is the time average of the I_{sat} signal), (ii) the interval $2.75\sigma - 3.5\sigma$, and (iii) the interval $3.5\sigma - 4.25\sigma$. In the following, these three scenarios are dubbed "case 1", "case 2", and "case 3", respectively. The three trigger windows result in blobs with different density peak values n_0, with $n_0/n_{bg} \approx 0.85, 1.0, 1.9$ for the three cases, where n_{bg} is the background plasma density at the reference probe position. These blobs are found to have different velocities and internal stability properties. For the three cases, the blob profiles at the detection time $t = 0$ are shown in Figs. 2.

The simulations are initialized according to the experimental measurements. The back-

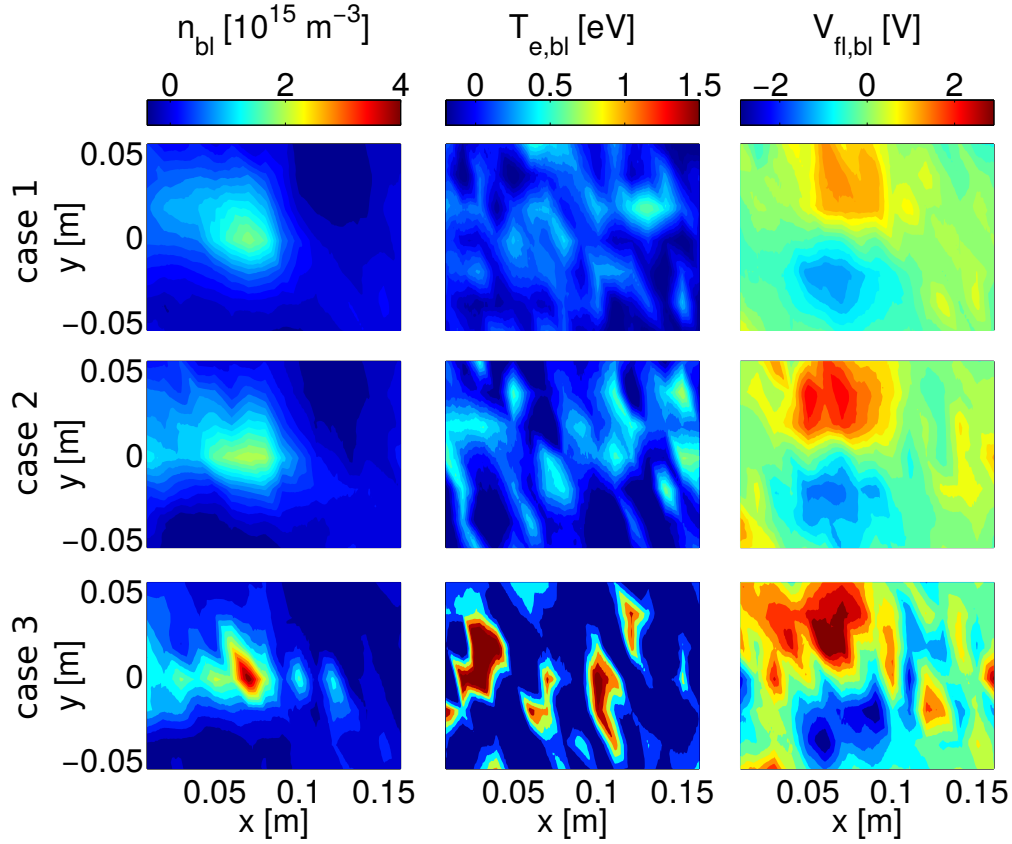

FIG. 2. Plasma density (first column), electron temperature (second column), and floating potential (third column) at detection time $t = 0$, for "case 1" (first row), "case 2" (second row), and "case 3" (third row) conditionally averaged blobs, from which have been subtracted the backgrounds.

ground profile of n and T_e are evaluated as the median value of the time-dependent signal reconstructed from the fit of the $I - V$ curves, and are shown in Fig. 1(b-c). As the dependence of the background profiles on the y coordinates is weak, they are fitted with expressions that depend only on x;

$$n_{bg}(x) = \alpha(\beta x)^{\gamma} + \delta \tag{20}$$

$$T_{e,bg}(x) = \epsilon \cdot \exp(\zeta x) \tag{21}$$

where $\alpha = -4.2 \cdot 10^{17}\,\mathrm{m}^{-3}$, $\beta = 1\,\mathrm{m}^{-1}$, $\gamma = 2.9$, $\delta = 2.5 \cdot 10^{15}\,\mathrm{m}^{-3}$, $\epsilon = 2.8\,\mathrm{eV}$, and $\zeta = -5.9\,\mathrm{m}^{-1}$. We note that the measurements of the plasma quantities are taken on a poloidal plane at a distance of approximatively 3 cm from the limiter and no experimental information is available on the parallel dependence of the profiles. This introduces an uncertainty in setting the z dependence of the equilibrium profiles (and blob initial conditions) in the

three-dimensional codes. However, in previous TORPEX experiments it has been observed that the plasma density background profile is approximatively flat along z, except for a drop in the proximity of the limiter[35]. Therefore, as suggested in Ref. [11], a density source

$$S(x,z) = n_{bg}(x) \cdot \frac{10 \exp\left(10|z-\pi|/\pi\right)}{\pi \left[\exp\left(10\right) - 1\right]} \tag{22}$$

is introduced in BOUT++3D and TOKAM3X. It follows that the source term to be used in BOUT++2D is $S_n = n_{bg}(x)/\pi$. In GBS we linearize the model equations, and, therefore, there is no need to introduce plasma sources. On the other hand, we have to impose the density background, and we choose to impose the one that is produced by using the source of Eq. (22) in BOUT++3D. In HESEL there are no plasma sources, and n_{bg} is imposed at $t = 0$ accordingly to Eq. (20). For the electron background temperature profile, we note that in BOUT++2D, BOUT++3D, and TOKAM3X, the electron dynamics is assumed to be isothermal. Therefore, in these models, a uniform background temperature is imposed, and a sensitivity study of $T_{e,bg}$ is performed (see Sec. V). On the other hand, in GBS and HESEL, $T_{e,bg}$ is expressed accordingly with Eq. (21), and it is assumed constant along z. Moreover, we note that HESEL describes finite ion temperature effects. Assuming the ion temperature as the ambient temperature (which approximatively corresponds to the neutral temperature), an uniform $T_i = 0.025\,\mathrm{eV}$ is imposed at $t = 0$.

Finally, the background profiles of ϕ, ω, $v_{\parallel i}$ and $v_{\parallel e}$ are obtained by imposing Bohm's boundary conditions at the limiter plate and assuming no net background current flowing to the limiter, as discussed in Ref. [11].

The blob initial conditions are set by using the conditionally averaged profiles at the detection time $t = 0$. The experimental profiles of n_{bl}, $T_{e,bl}$, and $V_{fl,bl}$ have been fitted, imposing a monopolar structure in the poloidal plane for n_{bl} and $T_{e,bl}$, and a dipolar structure

for $V_{fl,bl}$:

$$n_{bl}(x,y) = n_0 \cdot \exp\left[-\left(\frac{(x-x_0)}{\sigma_{n,x}}\right)^2 - \left(\frac{y}{\sigma_{n,y}}\right)^2\right] \tag{23}$$

$$T_{e,bl}(x,y) = T_0 \cdot \exp\left[-\left(\frac{(x-x_0)}{\sigma_{T,x}}\right)^2 - \left(\frac{y}{\sigma_{T,y}}\right)^2\right] \tag{24}$$

$$\begin{aligned} V_{fl,bl}(x,y) = {} & V_1 \cdot \exp\left[-\left(\frac{(x-x_0)}{\sigma_{V,x,1}}\right)^2 - \left(\frac{y-y_1}{\sigma_{V,y,1}}\right)^2\right] \\ & + V_2 \cdot \exp\left[-\left(\frac{(x-x_0)}{\sigma_{V,x,2}}\right)^2 - \left(\frac{y-y_2}{\sigma_{V,y,2}}\right)^2\right] \end{aligned} \tag{25}$$

where $x_0 = 0.07\,\mathrm{m}$ and the value of the other parameters appearing in Eqs. (23-25) are summarized in Table I for the three cases.

	case 1	case 2	case 3
$n_0\,[10^{15}\,\mathrm{m}^{-3}]$	1.975 ± 0.135	2.335 ± 0.325	4.395 ± 0.855
$\sigma_{n,x}$ [cm]	2.20 ± 0.20	2.40 ± 0.30	1.65 ± 0.45
$\sigma_{n,y}$ [cm]	2.40 ± 0.20	2.10 ± 0.20	1.75 ± 0.25
T_0 [eV]	0.345 ± 0.065	0.960 ± 0.250	1.730 ± 0.280
$\sigma_{T,x}$ [cm]	1.05 ± 0.15	1.05 ± 0.25	0.80 ± 0.20
$\sigma_{T,y}$ [cm]	3.65 ± 1.05	1.45 ± 0.25	2.85 ± 0.95
V_1 [V]	2.330 ± 0.170	4.600 ± 0.740	4.715 ± 0.405
$\sigma_{V,x,1}$ [cm]	3.55 ± 0.25	3.25 ± 0.25	4.95 ± 0.35
y_1 [cm]	2.55 ± 0.25	2.60 ± 0.20	1.15 ± 0.35
$\sigma_{V,y,1}$ [cm]	2.95 ± 0.05	3.10 ± 0.20	4.90 ± 0.60
V_2 [V]	-1.540 ± 0.140	-2.350 ± 0.550	-6.155 ± 0.965
$\sigma_{V,x,2}$ [cm]	3.10 ± 0.20	2.75 ± 0.35	2.95 ± 0.45
y_2 [cm]	-2.10 ± 0.40	-0.50 ± 0.80	-2.45 ± 0.15
$\sigma_{V,y,2}$ [cm]	4.00 ± 0.30	4.75 ± 0.45	2.50 ± 0.30

TABLE I. Parameters used to initialize the seeded blob simulations, derived by fitting the experimental measurements using Eqs. (23-25).

The expressions of n_{bl} and $V_{fl,bl}$ in Eqs. (23) and (25) are relatively well supported by the

experimental measurements. On the other hand, the fitting of $T_{e,bl}$ using Eq. (24) is only partially justified, due to the high uncertainties affecting the measurements (see Fig. 2). Because of these uncertainties, we also impose $\phi_{bl} \approx V_{fl,bl}$, neglecting the ΛT_e term (previous studies show that the ΛT_e term increases the blob spinning[36]). The three-dimensional initial profiles are obtained by using Bohm's boundary conditions at the limiter, and assuming that n_{bl}, $T_{e,bl}$, and ϕ_{bl} are constant along the parallel direction, while $v_{\parallel e,bl}$ and $v_{\parallel i,bl}$ are a linear function of z. We note that in the isothermal models $T_{e,bl} = 0$ is imposed. Finally, we enforce $\omega_{bl} = \nabla_\perp^2 \phi_{bl}$. The influence of the approximations introduced to initialize the seeded blob simulations on the numerical results is discussed in Sec. V.

The seeded blob motion is simulated on a time interval that is equal to the experimental blob correlation time, i.e. approximatively $50\,\mu$s. Longer simulations are not useful for comparison with the experiments, because the coherence of the conditionally averaged blob is completely lost on longer timescales.

To compare the numerical simulations against experimental measurements, we focus our attention on the blob radial and vertical motion. The position of the blob is computed as follows. First, for the simulation results, the blob ion saturation density current profile is computed as

$$j_{bl}(x,y,t) = \frac{1}{2}[n_{bg}(x) + n_{bl}(x,y,t)]\sqrt{T_{e,bg}(x) + T_{e,bl}(x,y,t)} - \frac{1}{2} n_{bg}(x)\sqrt{T_{e,bg}(x)} \tag{26}$$

while for the experimental results it is simply given by

$$j_{bl}(x,y,t) = \frac{I_{sat}(x,y,t) - \langle I_{sat}(x,y,t)\rangle_t}{A} \tag{27}$$

where $I_{sat}(x,y,t)$ is the measured ion saturation current, $\langle - \rangle_t$ denotes the median value in time, and A is the projected area of the single-sided LP probe. Second, the j_{bl} signal is averaged in space, $j_{bl}(t) = \langle j_{bl}(x,y,t)\rangle_{x,y}$, where $\langle - \rangle_{x,y}$ denotes averaging along the x and y coordinates on the entire physical domain. Third, we identify the surface $S(t)$ which satisfies $\langle j_{bl}(x,y,t)\rangle_{S(t)} = 0.2 \cdot j_{bl}(t)$, where $\langle - \rangle_{S(t)}$ denotes the average carried out on the domain defined by $S(t)$. Finally, the position of the blob is identified as the geometric center of the

surface S:

$$x_{bl}(t) = \frac{\iint_{S(t)} x dx dy}{\iint_{S(t)} dx dy}$$
$$y_{bl}(t) = \frac{\iint_{S(t)} y dx dy}{\iint_{S(t)} dx dy} \tag{28}$$

The use of this procedure allows us to reduce the sensitivity of the results to the noise present in the profiles. The radial and vertical velocities of the blob are simply defined as $v_x(t) = dx_{bl}(t)/dt$ and $v_y(t) = dy_{bl}(t)/dt$. To exemplify the use of this procedure, in Fig. 3 we consider the experimental measurements associated with blobs at the three times $t = 0$, $t = 24\,\mu s$, and $t = 48\,\mu s$. The black contours represent the boundaries of the surfaces S and the black crosses denote the blob positions, x_{bl} and y_{bl}.

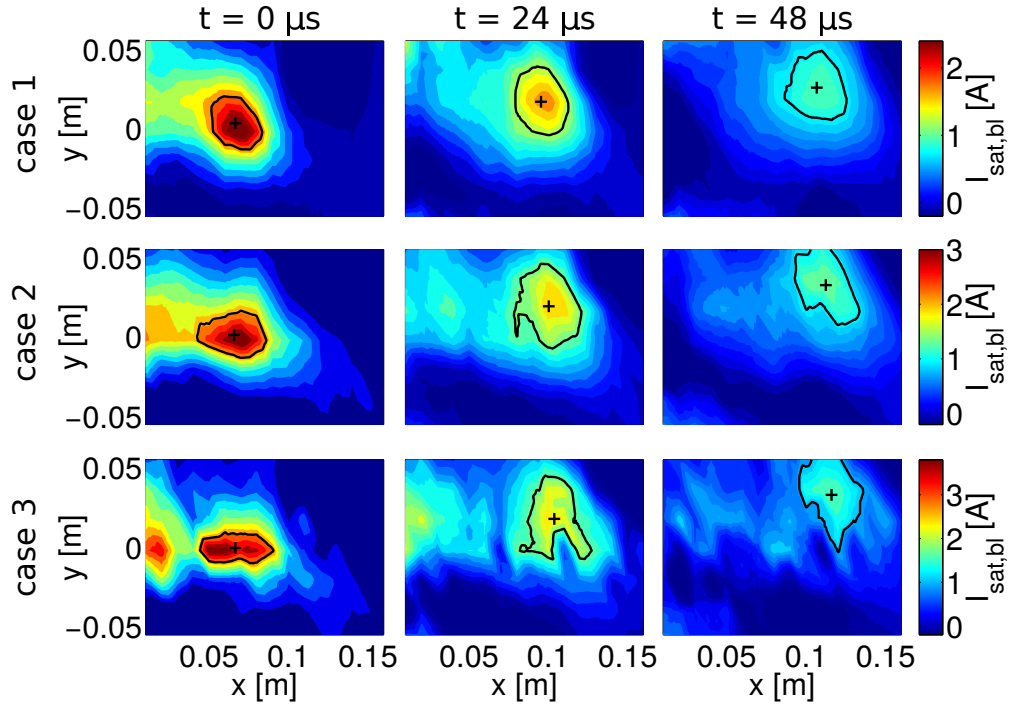

FIG. 3. Experimentally measured I_{sat} profiles, from which have been subtracted the background, at $t = 0$ (first column), $t = 24\,\mu s$ (second column), and $t = 48\,\mu s$ (third column), for the "case 1" (first row), "case 2" (second row), and "case 3" (third row) blobs. The black contours represent the boundaries of the surfaces which satisfy $\langle j_{bl}(x, y, t)\rangle_{S(t)} = 0.2 \cdot j_{bl}(t)$ and the black crosses denote the blob positions x_{bl} and y_{bl}.

In order to justify the approach of validating seeded blob simulations against conditionally-

averaged experimental measurements, we have to ensure that the velocity of conditionally-averaged, turbulence-generated blobs does not significantly differ from the velocity of a seeded blob. This is achieved as follows. Applying the conditional average technique described in Sec. II to a long two-dimensional fully turbulent GBS simulation, we obtain the conditionally-averaged profiles associated with blobs, and we use these profiles to initialize a two-dimensional seeded blob simulation. The comparison of the velocities obtained from the seeded blob simulation and the conditionally-averaged blob, which is not displayed here, show that the difference between the two velocities is to within an error of 10%.

V. SENSITIVITY STUDIES

In order to compare the simulation results among each other and against the experimental measurements, four sensitivity scans have been performed. We first investigate the sensitivity of the simulation results to the input parameters and initial conditions. Second, we focus our attention on the influence of the equilibrium electron temperature profiles on the numerical results. Third, we analyze the impact of the electron temperature dynamics on the blob motion. Finally, we study the sensitivity of the simulation results to the numerical parameters, such as the diffusion coefficients introduced in GBS and TOKAM3X.

To estimate the effect of the uncertainties found in setting the initial conditions (discussed in Sec. IV) on the simulation results, we first estimate the confidence intervals of the fitting parameters (Table I). Second, we perform a sensitivity scan of the blob size (σ_x and σ_y coefficients) and of the peak-to-peak value of its dipolar potential, as they are expected to be the parameters that affect the blob velocity the most. More precisely, we perform five simulations for each of the three cases: one simulation, dubbed standard simulation, initialized with the centered fitting parameters, two simulations setting the size of the blob using the minimum and maximum values within the confidence interval of the fitting parameters, and two other simulations with the minimum and maximum peak-to-peak values of the dipolar profile of the plasma potential. Third, we compute the maximum of the difference between the standard simulation and the other four simulations, and we use this as the measure of the uncertainty affecting the numerical results.

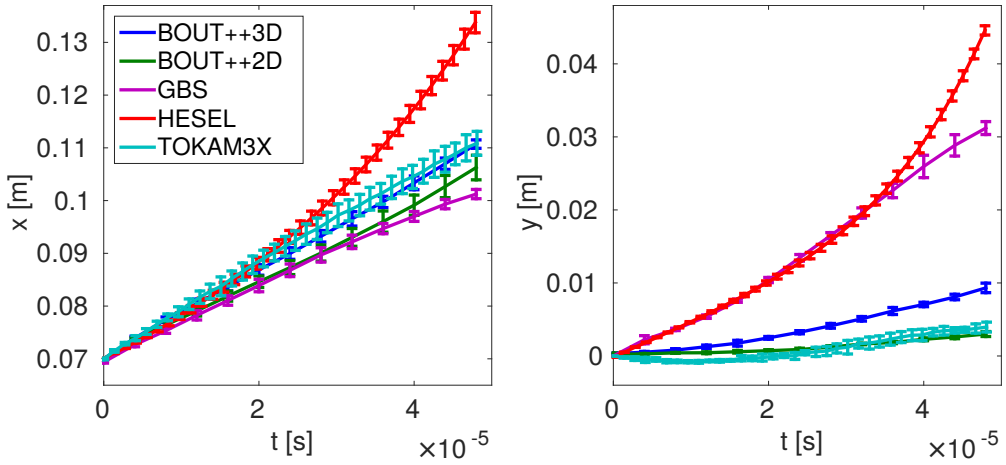

FIG. 4. Radial (left) and vertical (right) position of the blob as function of time for "case 1", with errorbars representing the uncertainties affecting the numerical results due to the uncertainties on the initial conditions.

The results of the sensitivity scan for the "case 1" blob are shown in Fig. 4, where the errorbars represent the evaluated uncertainties. It is evident that the uncertainties affecting the radial and vertical position of the blobs are relatively small, which ensures that the uncertainties on the blob initial conditions do not strongly affect the simulation results. Similar results (not shown) are obtained for "case 2" and "case 3".

Next, we perform a sensitivity scan of the electron temperature background value. This is motivated by the fact that, while BOUT++3D, BOUT++2D, and TOKAM3X assume a uniform $T_{e,bg}$, the experimental temperature background profile shows a strong radial variation.

The results of this sensitivity study are presented in Fig. 5. BOUT++3D, BOUT++2D, and TOKAM3X are used to carry out two simulations each, one with $T_{e,bg} = 2.8\,\text{eV}$ ($T_{e,bg}$ value at $x = 0.0\,\text{cm}$, corresponding to the maximum value of $T_{e,bg}$ over the considered domain) and one with $T_{e,bg} = 1.85\,\text{eV}$ ($T_{e,bg}$ value at $x = 0.07\,\text{cm}$, corresponding to the $T_{e,bg}$ value at the position where the blob is initialized). Moreover, two simulations are performed with GBS, one imposing a uniform $T_{e,bg} = 2.8\,\text{eV}$, and one with $T_{e,bg}$ set according to Eq. (21).

Figure 5 shows that the radial velocity of the blob is strongly affected by $T_{e,bg}$ (a larger $T_{e,bg}$

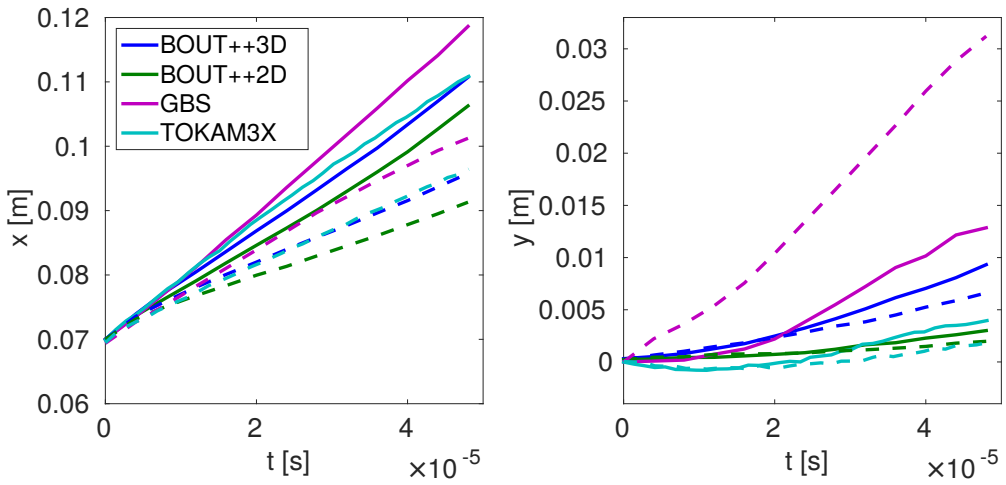

FIG. 5. Radial (left) and vertical (right) position of the blob as function of time for "case 1". Solid curves represent the simulation results with $T_{e,bg} = 2.8\,\text{eV}$, dashed curves consider $T_{e,bg} = 1.85\,\text{eV}$ for BOUT++3D, BOUT++2D, and TOKAM3X and $T_{e,bg}$ given by Eq. (21) for GBS.

leads to a larger radial velocity). Furthermore, GBS simulations point out that the blob radial motion is faster for $T_{e,bg} = 2.8\,\text{eV}$ than for the experimental $T_{e,bg}$ profile. Regarding the vertical motion of the blob, we observe that the radial variation of $T_{e,bg}$ strongly impacts the blob dynamics, while varying a uniform $T_{e,bg}$ value has a minor impact. In fact, when a radial dependent profile of $T_{e,bg}$ is considered, by imposing Bohm's boundary conditions at the limiter and no net parallel background current flowing to the target, we obtain a radially dependent electrostatic background potential, which leads to a positive $v_{E\times B}$ in the vertical direction. Similar results are obtained for the "case 2" and "case 3" blobs. Consequently, the $T_{e,bg}$ profile considerably affects the simulation results. In Sec. VI this has to be taken into account in the comparison of the simulation results among each other and with experimental measurements.

Then, we simulate with the GBS code an isothermal blob (i.e., we impose $T_{e,bl} = 0$ at all times), an initially thermalized blob (i.e., we impose $T_{e,bl} = 0$ at $t = 0$ and then let the blob temperature evolve), and an initially hot blob [i.e., we impose $T_{e,bl} = T_{e,bl}(x, y)$ at $t = 0$, accordingly to Eq. (24), and then let the blob temperature evolve]. A uniform $T_{e,bg} = 2.8\,\text{eV}$ is imposed. This is motivated by two things. First, as discussed in Sec. IV, high uncertainties are affecting the experimental measurements of the electron temperature.

Second, in BOUT++3D, BOUT++2D, and TOKAM3X the blob is assumed isothermal, while in GBS and HESEL the electron temperature is evolved. In Fig. 6 we present the

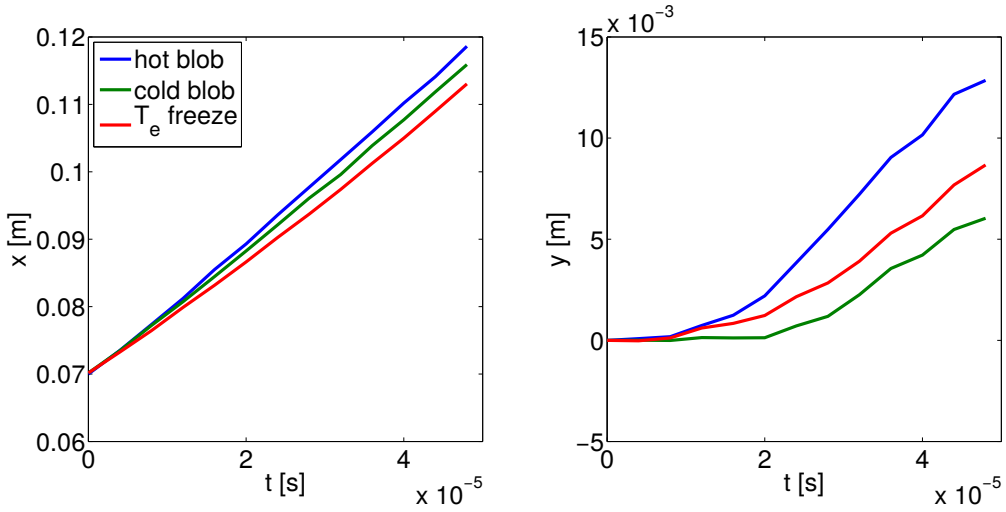

FIG. 6. Radial (left) and vertical (right) position of the blob as function of time, obtained from GBS simulations of "case 1" with $T_{e,bg} = 2.8\,\mathrm{eV}$. The blue curves correspond to an initially hot blob [i.e., $T_{e,bl} = T_{e,bl}(x, y)$ at $t = 0$, as in Eq. (24)], the green curves correspond to an initially thermalized blob (i.e., $T_{e,bl} = 0$ at $t = 0$ and then letting the blob temperature evolve), and the red curves correspond to an isothermal blob (i.e., imposing $T_{e,bl} = 0$ at all times).

results of this study. Considering the radial motion, we observe that the isothermal blob is the slowest one, while the hot blob is the fastest. However, the motion of the blob is only slightly affected by temperature effects. Moreover, Fig. 6 shows that the impact of the isothermal blob assumption on the blob vertical velocity is very small. This indicates that the presence of a radially-varying $T_{e,bg}$ profile is the main drive of the vertical motion, as discussed above.

Finally, we note that all the simulations used for this paper are converged with respect to the temporal and spatial discretization. Moreover, performing several sensitivity scans, it has been verified that the values of the numerical parameters, such as the diffusion coefficients introduced in GBS and TOKAM3X, do not significantly affect the simulation results.

VI. ANALYSIS AND VALIDATION OF THE SIMULATION RESULTS

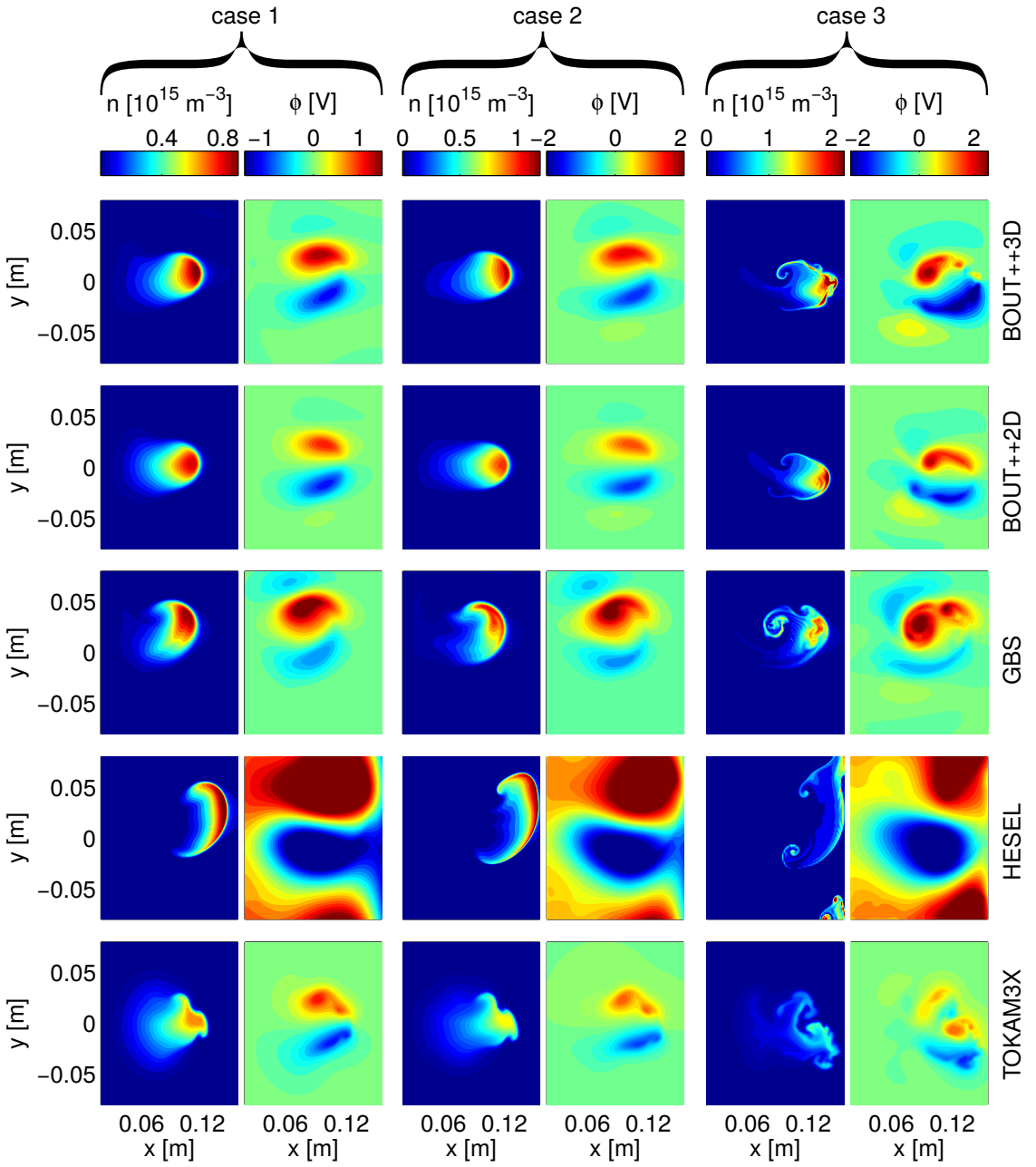

FIG. 7. Plasma density and electrostatic potential, for the "case 1", "case 2", and "case 3" blobs, simulated with BOUT++2D, BOUT++3D, GBS, HESEL, and TOKAM3X, at $t = 48\,\mu$s. We note that for BOUT++2D and for HESEL the line averaged quantities $n(x, y)/2$ and $\phi(x, y)$ are represented, while the profiles of $n(x, y, z)$ and $\phi(x, y, z)$ are displayed for the three-dimensional models at the simulated poloidal plane closest to the limiter.

First, focusing our attention on the qualitative analysis of the blob simulation results, we present in Fig. 7 the two-dimensional poloidal profiles of plasma density and electrostatic potential associated with "case 1", "case 2", and "case 3" blobs at $t = 48\,\mu$s, for the five simulation models. We consider $T_{e,bg} = 2.8\,$eV in the isothermal and Eq. (21) in the non-isothermal models. Several observations can be made from these results.

(i) Noticeable differences exist between the "case 1" and "case 2" blobs, and the "case 3". In particular, the size of the "case 3" blob is significantly smaller than in the two other cases. This leads to steeper gradients and stronger secondary instabilities, consistent with the numerical results.

(ii) The BOUT++2D results are qualitatively similar to the ones from BOUT++3D, the main difference being the amplitude of the density profiles. This is due to the fact that in BOUT++2D line-averaged quantities are evolved and plotted, while for BOUT++3D snapshots on a poloidal plane close to the limiter are shown, where the blob density is smaller than at the center of the device.

(iii) Comparing the results of BOUT++3D, GBS, and TOKAM3X, although we observe a similar global evolution of the blobs, some differences in the details of the structures are apparent. In TOKAM3X the blobs are subject to fingering effects, not visible in the other simulations. The shape of the BOUT++3D blobs is rounder than in GBS and the blob tails are less pronounced in GBS (tests show that this is related to the plasma-neutral collisions, not taken into account by the other three-dimensional models). Moreover, we note that the blobs simulated with GBS show an upward motion, and are spinning counterclockwise. The upward motion is related to the $\mathbf{E} \times \mathbf{B}$ vertical motion due to the radial dependence of the electron temperature background, as discussed in Sec. V. The spinning occurs because of effects of the evolving electron temperature on the blob plasma potential, which is consistent with the observations in Ref. [36].

(iv) Focusing on the HESEL results, we note that the blobs are more "mushroom-like" and show a completely different evolution than in the other four models. As discussed in Ref. [11], one can infer that this is related to the HESEL assumption that diamagnetic

currents are predominately closed through polarization currents.

The analysis of the differences among the five models helps us understand the results of the validation of the simulation results against the experimental measurements. The radial and vertical blob velocities produced by the simulations and as measured from the experiment are plotted versus time in Figs. 8 and 9.

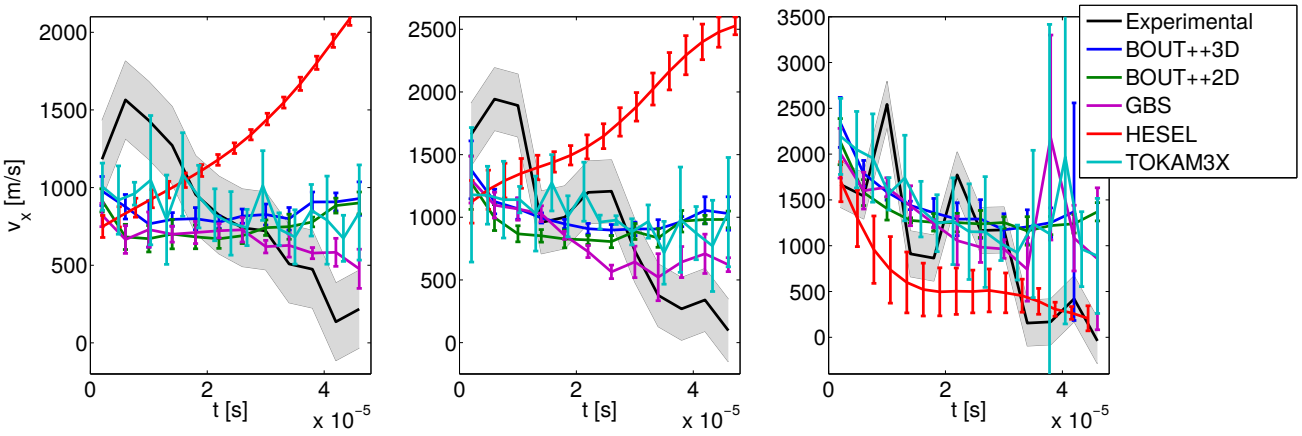

FIG. 8. Radial velocity of the blob as function of time for "case 1" (left), "case 2" (middle), and "case 3" (right), obtained from numerical simulations and experimental measurements (the gray shaded region represents the experimental uncertainty due to the finite spatial resolution of the probes).

Regarding the experimental measurement of the radial velocity, despite some fluctuations mainly due to experimental uncertainties, it is visible that blobs decelerate as they move outwards, for each of the three cases. The radial velocity of the blobs simulated with BOUT++3D, BOUT++2D, GBS, and TOKAM3X also decreases in time. However, particularly in "case 1" and "2", the blob decelleration is weaker in the simulation results than in experiments, and the initial velocity peak is not well captured. On the other hand, the radial blob velocity simulated with HESEL shows a completely different evolution. In fact, while moving outwards, the HESEL "case 1" and "case 2" blobs accelerate significantly, while the "case 3" blob decelerates.

To perform a quantitative comparison between experiments and numerical results, and to

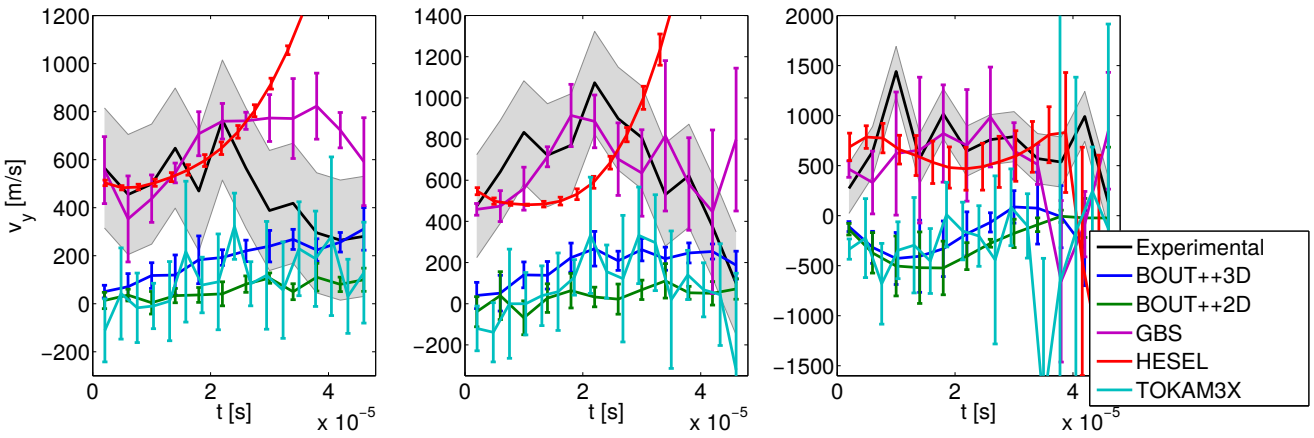

FIG. 9. Vertical velocity of the blob as function of time for "case 1" (left), "case 2" (middle), and "case 3" (right), obtained from numerical simulations and experimental measurements (the gray shaded region represents the experimental uncertainty due to the finite spatial resolution of the probes).

gain a deeper insight on the blob dynamics, we average the experimental and the simulated radial blob velocities between $t = 0$ and $t = 48\,\mu$s, for the three cases, and we theoretically predict the radial blob velcity according to Ref. [20]:

$$v_x = \frac{\sqrt{\frac{2a}{R}}c_s}{1 + \frac{1}{\rho_s^2 L_\parallel}\sqrt{\frac{R}{2}}a^{5/2} + \frac{\nu_{\rm in}\sqrt{Ra}}{\sqrt{2}c_s}} \frac{n_0}{n_{bg} + n_0} \tag{29}$$

where $a = \sqrt{\ln 2}\sigma_{n,y}$ is the vertical size of the blob, $\rho_s \approx \sqrt{T_{e,bg} m_i}/(eB)$ is the ion Larmor radius, $c_s \approx \sqrt{T_{e,bg}/m_i}$ is the ion sound speed, and $n_0/(n_{bg} + n_0)$ is the ratio between the peak density value of the blob, n_0, and the total density, $n_{bg} + n_0$. The three terms in the denominator represent possible closures of the diamagnetic current due to, respectively, the ion polarization current, the parallel current to the sheath, and the ion-neutral collisions (the latter is neglected in the following due to the low value of ν_{in}). The $n_0/(n_{bg} + n_0)$ term represents the slowing down of the blob due to a finite background density. Equation (29) is derived under the assumption of isothermal evolution.

In Table II we summarize the results of our analysis. First, considering the two background electron temperatures $T_{e,bg} = 1.85\,$eV and $T_{e,bg} = 2.8\,$eV, we compute the velocities theoretically predicted by using Eq. (29). We compute both the expected velocity from the full scaling in Eq. (29) ("Analytical scaling"), and the expected velocity from the ion-

polarization closure scaling when an halved ballooning instability drive is considered, which corresponds to $v_x = \sqrt{a/R} c_s n_0/(n_{bg} + n_0)$ ("Polarization closure"). Second, averaging in time the radial velocities, we list the BOUT++2D, BOUT++3D, and TOKAM3X results corresponding to $T_{e,bg} = 1.85\,\mathrm{eV}$ and $T_{e,bg} = 2.8\,\mathrm{eV}$. For GBS, simulations with a uniform $T_{e,bg} = 2.8\,\mathrm{eV}$ background and considering an isothermal blob (i.e., $T_{e,bl} = 0$ at all times) are listed. Moreover, we present the GBS and HESEL results when the experimental background temperature profile are used and the blob temperature is evolved. Finally, the experimental radial velocity measurements are averaged in time, to obtain the values presented in the last row of Table II. Several observations can be made from these results.

(i) The velocities obtained for $T_{e,bg} = 2.8\,\mathrm{eV}$ from BOUT++3D, GBS with isothermal electrons, and TOKAM3X are very similar. It follows that the three models are equally able to predict the radial velocity of the blobs. Within the uncertainties affecting the measured quantities used as input parameters, they are consistent with experimental observations for "case 1" and "case 2", while the "case 3" experimental measurements do show a smaller velocity with respect to the simulations. This difference is due to the blob motion in late part of the considered time interval, when the blob loses its coherence and the difference between experimental measurements and simulation results increases, as shown in Fig. 8.

(ii) BOUT++2D gives a radial velocity that is slightly smaller than the one computed with the three-dimensional isothermal models. Previous comparisons between two-dimensional and three-dimensional simulation results[12] have shown that the density drop in the three-dimensional simulations is larger than the one estimated to derive the two-dimensional models. This leads to smaller parallel sheath currents and, therefore, faster blob dynamics in the three-dimensional simulations. However, the difference between BOUT++2D and BOUT++3D results are relatively small, indicating that the sheath dissipation closure represents well the considered experiments. This is consistent with previous experimental investigations, from which it has been concluded that for similar TORPEX experimental scenarios the parallel currents play an important role in setting the blob motion[20,37,38].

(iii) The "case 1" and "case 2" blobs simulated with HESEL produce radial velocities

that are much larger than the ones observed experimentally. This leads us to conclude that, for the present experimental scenario, the weak sheath formulation combined with the vorticity advection closure is not a good representation of the plasma dynamics, consistently with point (ii). It is emphasized that this result concerns only the considered experimental scenario, and it is not generally true.

(iv) The analysis of "case 3" HESEL results shows a velocity that is smaller than both the experimental velocity and the velocity resulting from the other models. This may be due to the fact that the blob completely loses its coherence through the simulation, as can be observed in Fig. 7.

(v) The simulation results obtained with GBS considering the experimental temperature background show a radial velocity that is slightly smaller than the measured one for "case 1" and "case 2", while it is slightly higher for "case 3". It could appear surprising at first sight that the experiments agree better with the isothermal models than with the results of the non-isothermal GBS simulations. However, Fig. 8 shows that this is due to a fortuitous event: the differences in the radial velocity between experimental measurements and isothermal simulations in the first and second halves of the simulations are canceling out, giving an apparently better agreement of the averaged radial velocities.

(vi) Comparing our isothermal simulation results with the analytical scaling derived from the isothermal estimate presented in Ref. [20], we observe that Eq. (29) underestimates the blob radial velocity. In the appendix of Ref. [37] and in Ref. [39] other possible blob velocity scalings are discussed, for which it is assumed that the blob is subject to a Kelvin-Helmholtz instability. These scalings produce results which differ from Eq. (29) when low values of $n_0/(n_{bg}+n_0)$ are considered. In particular, they give larger velocities than the ones predicted by using Eq. (29), which are closer to the numerical results of the isothermal simulations. Additionally, assuming that the analytical scaling of Eq. (29) underestimates the blob radial velocity because of the small value of $n_0/(n_{bg} + n_0)$, and comparing the HESEL results with the "Polarization closure" row in Table II, we conclude that the HESEL model should be able to properly describe the blob dynamics in cases where diamagnetic currents are predominantly closed through polarization currents.

Considering the experimental vertical motion, we observe that the blobs move in TORPEX with positive, almost constant, velocity. The dynamics of the blobs simulated with GBS is consistent with the experimental measurements; the HESEL model, which assume a non-isothermal background accordingly with Eq. (21), presents a vertical velocity that is initially consistent with experimental measurements and diverges later from the experimental results; while the other models are not in agreement with the experimental measurements. This reflects the fact that the vertical blob motion is mostly driven by a background $v_{E\times B}$ flow, as discussed in Sec. V.

VII. CONCLUSIONS

In this paper we present numerical results obtained from seeded blob simulations carried out with five different models, which are validated against the experimental data obtained from the TORPEX device. The models differ because of a number of assumptions used to simplify the drift-reduced Braginskii equations, such as the hypothesis of cold ions, isothermal electrons, or negligible electron inertia. Moreover, some of the models make use of infinite aspect ratio approximation. In addition to three-dimensional models, we also consider two-dimensional models, based on different closures of the parallel currents on the vessel walls.

The comparison between the results of the different models and the experiments allow us to identify the most important physics elements that play a role in setting the blob velocity. For the present experimental scenario, we show that the vorticity advection closure, such as the one implemented in HESEL, is not able to correctly reproduce the plasma dynamics associated with the blobs, while the sheath dissipation closure, such as the one implemented in BOUT++2D, is in agreement with the three-dimensional simulations and experimental results. This is consistent with previous experimental analysis, whereby it has been showed that, in typical TORPEX hydrogen plasmas, parallel currents are important in setting the radial velocity of blobs. To properly validate the HESEL model, one would need to consider plasmas with higher ion mass or blobs with a smaller size, for which it has been shown that the parallel current contribution is negligible[37].

Moreover, we also observe that the value of the background electron temperature is impor-

tant in setting the radial velocity of blobs, meaning that an accurate measurement of this quantity is necessary to perform reliable simulations. Moreover, comparing the results of the five codes between each other, we conclude that the radial dependence of the electron temperature background plays a role in determining the correct vertical motion of the blobs, while the evolution of the electron temperature is only necessary to describe its spinning. We also showed that the electron inertia, the Boussinesq approximation, and the infinite aspect ratio limit have a minor importance in determining the blob velocity.

The results presented in this paper provide us with a better understanding of the blob dynamics, and increase the reliability of the models used to carry out the seeded blob simulations. The experimental scenario presented in this paper constitutes an ideal test bed also for future benchmarks and the validation of seeded blob simulations, thanks to the measurements available, which allow accurate initialization of the simulations and detailed comparisons with the numerical results. The magnetic configuration that we consider facilitates considerably the analysis and the interpretation of the experimental and simulation results.

This work represents a fundamental step towards the validation of full turbulence simulations against experimental measurements in more complex geometries, such as a tokamak SOL.

ACKNOWLEDGMENTS

The authors gratefully acknowledge useful discussions with G. Ciraolo, N. Fedorczak, N. Loureiro, and N. Nace. The simulations presented herein were carried out in part using the Plasma HEC Consortium EPSRC Grant No. EP/L000237/1; in part using the HELIOS supercomputer system at Computational Simulation Centre of International Fusion Energy Research Centre (IFERC-CSC), Aomori, Japan, under the Broader Approach collaboration between Euratom and Japan, implemented by Fusion for Energy and JAEA; in part at the Swiss National Supercomputing Centre (CSCS) under Projects ID s544 and s549; in part using the HPC resources of IDRIS, under the allocation 2014242 made by GENCI; and in part using the HPC resources of Aix-Marseille Université financed by the project Equip@Meso (ANR-10-EQPX-29-01) of the program "Investissement d'Avenir" supervised

by the Agence Nationale pour la Recherche. This work was carried out within the framework of the EUROfusion Consortium, being supported in part by the Swiss National Science Foundation and in part by the Euratom research and training programme 2014-2018 under the grants agreement No 633053 and WP14-FRF-EPFL/Theiler. The views and opinions expressed herein do not necessarily reflect those of the European Commission.

REFERENCES

[1]E. D. C. T. Physics), W. H. C. C. D. Modelling), , Y. K. C. P. Edge), V. M. c.-C. T. Physics), , T. O. c.-C. P. Edge), A. P. c.-C. C. D. Modelling), G. Bateman, J. Connor, J. C. (retired), T. Fujita, X. Garbet, T. Hahm, L. Horton, A. Hubbard, F. Imbeaux, F. Jenko, J. Kinsey, Y. Kishimoto, J. Li, T. Luce, Y. Martin, M. Ossipenko, V. Parail, A. Peeters, T. Rhodes, J. Rice, C. Roach, V. Rozhansky, F. Ryter, G. Saibene, R. Sartori, A. Sips, J. Snipes, M. Sugihara, E. Synakowski, H. Takenaga, T. Takizuka, K. Thomsen, M. Wade, H. Wilson, I. T. P. T. Group, I. C. D. Group, Model, I. P. Group, and E. Topical, Nuclear Fusion **47**, S2 (2007).

[2]D. A. D'Ippolito, J. R. Myra, and S. J. Zweben, Physics of Plasmas **18**, 060501 (2011).

[3]S. I. Krasheninnikov, D. A. D'Ippolito, and J. R. Myra, Journal of Plasma Physics **74**, 679 (2008).

[4]O. E. Garcia, N. H. Bian, V. Naulin, A. H. Nielsen, and J. J. Rasmussen, Physics of Plasmas **12**, 090701 (2005).

[5]A. Y. Aydemir, Physics of Plasmas **12**, 062503 (2005).

[6]N. Bian, S. Benkadda, J.-V. Paulsen, and O. E. Garcia, Physics of Plasmas **10**, 671 (2003).

[7]D. A. D'Ippolito and J. R. Myra, Physics of Plasmas **10**, 4029 (2003).

[8]G. Q. Yu and S. I. Krasheninnikov, Physics of Plasmas **10**, 4413 (2003).

[9]S. Sugita, M. Yagi, S. I. Itoh, and K. Itoh, Plasma and Fusion Research **3**, 040 (2008).

[10]I. Furno, C. Theiler, D. Lançon, A. Fasoli, D. Iraji, P. Ricci, M. Spolaore, and N. Vianello, Plasma Physics and Controlled Fusion **53**, 124016 (2011).

[11]L. Easy, F. Militello, J. Omotani, B. Dudson, E. Havlíčková, P. Tamain, V. Naulin, and A. H. Nielsen, Physics of Plasmas **21**, 122515 (2014).

[12]F. D. Halpern, A. Cardellini, P. Ricci, S. Jolliet, J. Loizu, and A. Mosetto, Physics of Plasmas **21**, 13 (2014).

[13]B. Dudson, M. Umansky, X. Xu, P. Snyder, and H. Wilson, Computer Physics Communications **180**, 1467 (2009).

[14]P. Ricci, F. D. Halpern, S. Jolliet, J. Loizu, A. Mosetto, A. Fasoli, I. Furno, and C. Theiler, Plasma Physics and Controlled Fusion **54**, 124047 (2012).

[15]A. Nielsen, G. Xu, J. Madsen, V. Naulin, J. Juul Rasmussen, and B. Wan, Physics Letters A **379**, 3097 (2015).

[16]J. J. Rasmussen, A. H. Nielsen, J. Madsen, V. Naulin, and G. S. Xu, Plasma Physics and Controlled Fusion **58**, 014031 (2016).

[17]P. Tamain, H. Bufferand, G. Ciraolo, C. Colin, P. Ghendrih, F. Schwander, and E. Serre, Contributions to Plasma Physics **54**, 555 (2014).

[18]A. Fasoli, B. Labit, M. McGrath, S. H. Müller, G. Plyushchev, M. Podestà, and F. M. Poli, Physics of Plasmas **13**, 055902 (2006).

[19]I. Furno, F. Avino, A. Bovet, A. Diallo, A. Fasoli, K. Gustafson, D. Iraji, B. Labit, J. Loizu, S. H. Müller, G. Plyushchev, M. Podestà, F. M. Poli, P. Ricci, and C. Theiler, Journal of Plasma Physics **81**, 345810301 (2015).

[20]C. Theiler, I. Furno, P. Ricci, A. Fasoli, B. Labit, S. H. Müller, and G. Plyushchev, Physical Review Letters **103**, 065001 (2009).

[21]I. Furno, B. Labit, A. Fasoli, F. M. Poli, P. Ricci, C. Theiler, S. Brunner, A. Diallo, J. P. Graves, M. Podestà, and S. H. Müller, Physics of Plasmas **15**, 055903 (2008).

[22]I. Furno, B. Labit, M. Podestà, A. Fasoli, S. H. Müller, F. M. Poli, P. Ricci, C. Theiler, S. Brunner, A. Diallo, and J. Graves, Physical Review Letters **100**, 055004 (2008).

[23]S. I. Braginskii, *Transport Processes in a Plasma*, edited by M. A. Leontovich (Consultants Bureau Enterprise, New York, 1965) p. 205.

[24]A. Zeiler, J. F. Drake, and B. Rogers, Physics of Plasmas **4**, 2134 (1997).

[25]D. A. Russell, D. A. D'Ippolito, and J. R. Myra, Bulletin of the American Physical Society, 54th Annual Meeting of the APS Division of Plasma Physics, Vol. 57, No. 12 (2012), available at http://meetings.aps.org/link/BAPS.2012.DPP.BP8.159.

[26]G. Q. Yu, S. I. Krasheninnikov, and P. N. Guzdar, Physics of Plasmas **13**, 042508 (2006).

[27]K. Bodi, G. Ciraolo, P. Ghendrih, F. Schwander, E. Serre, and P. Tamain, in *38th EPS Conference on Plasma Physics*, P1.121 (Strasbourg, France, 2011).

[28]P. Stangeby, *The Plasma Boundary of Magnetic Fusion Devices*, Series in Plasma Physics and Fluid Dynamics (Taylor & Francis, 2000).

[29]A. Arakawa, Journal of Computational Physics **1**, 119 (1966).

[30]G. D. Byrne and A. C. Hindmarsh, Int. J. High Perform. Comput. Appl. **13**, 354 (1999).

[31]C. G. Theiler, *Basic Investigation of Turbulent Structures and Blobs of Relevance for Magnetic Fusion Plasmas*, Ph.D. thesis, SB, Lausanne (2011).

[32]G. E. Karniadakis, M. Israeli, and S. A. Orszag, Journal of Computational Physics **97**, 414 (1991).

[33]R. Donat and A. Marquina, Journal of Computational Physics **125**, 42 (1996).

[34]W. Fundamenski, O. E. Garcia, V. Naulin, R. Pitts, A. H. Nielsen, J. J. Rasmussen, J. Horacek, J. P. Graves, and J. E. Contributors, Nuclear Fusion **47**, 417 (2007).

[35]I. Furno, C. Theiler, V. Chabloz, A. Fasoli, and J. Loizu, Physics of Plasmas **21**, 012305 (2014).

[36]J. R. Myra, D. A. D'Ippolito, S. I. Krasheninnikov, and G. Q. Yu, Physics of Plasmas **11**, 4267 (2004).

[37]C. Theiler, I. Furno, A. Fasoli, P. Ricci, B. Labit, and D. Iraji, Physics of Plasmas **18**, 055901 (2011).

[38]I. Furno, M. Spolaore, C. Theiler, N. Vianello, R. Cavazzana, and A. Fasoli, Physical Review Letters **106**, 245001 (2011).

[39]J. T. Omotani, F. Militello, L. Easy, and N. R. Walkden, Plasma Physics and Controlled Fusion **58**, 014030 (2016).

T_e Backrgound	case 1 [m/s]			case 2 [m/s]			case 3 [m/s]		
	1.85 eV	2.8 eV	Eq (21)	1.85 eV	2.8 eV	Eq (21)	1.85 eV	2.8 eV	Eq (21)
Analytical scaling	420±40	670± 50	-	530±50	810±60	-	800±80	1170±90	-
Polarization closure	910±40	1100±50	-	990±70	1180±90	-	1280±100	1480±110	-
BOUT++2D	440	760±50	-	570	930±30	-	1000	1370±30	-
BOUT++3D	540	850±20	-	670	1020±20	-	1100	1460±130	-
TOKAM3X	560	870±60	-	710	1020±40		1030	1210±210	
GBS isothermal	-	890	-	-	1070	-	-	1520	-
GBS	-	-	660±10	-	-	790±40	-	-	1370±150
HESEL	-	-	1470±40	-	-	1850±70	-	-	650±200
Experimental	-	-	840±20	-	-	970±20	-	-	1030±20

TABLE II. Blob radial velocity for the three cases, computed with Eq. (29) and time-averaging simulations and experimental results.